Chemical Engineering Journal 425 (2021) 130620

Contents lists available at ScienceDirect

Chemical Engineering Journal

journal homepage: www.elsevier.com/locate/cej

Controllable synthesis and n-doping of $HMoO_x$ nanoparticle inks through simple photoreduction for solution-processed organic photovoltaics

Wusong Zha [a,b], Huimin Gu [b], Wei Pan [b], Xue Sun [b], Yunfei Han [b], Zhiyun Li [c], Xuefei Weng [c], Qun Luo [a,b,*], Shangfeng Yang [d], Chang-Qi Ma [a,b,*]

[a] School of Nano-Tech and Nano-Bionics, University of Science and Technology of China, Hefei 230026, PR China
[b] Printable Electronics Research Center, Suzhou Institute of Nano-Tech and Nano-Bionics, Chinese Academy of Sciences(CAS), Suzhou 215123, PR China
[c] Vacuum Interconnected Nanotech Workstation (Nano-X), Suzhou Institute of Nano-Tech and Nano-Bionics, Chinese Academy of Sciences (CAS), Suzhou 215123, China
[d] Department of Materials Science and Engineering Synergetic Innovation Center of Quantum Information & Quantum Physics, University of Science and Technology of China, Hefei 230026, PR China

ARTICLE INFO

Keywords:
Organic solar cells
Hole transporting layer
Solution-processable $HMoO_x$
Photoreduction

ABSTRACT

Solution-processable hole transporting layer (HTL) is one basis for the full-solution-processable fabrication of the organic solar cells (OSCs). Molybdenum oxide (MoO_x) is a widely used HTL and has the possibility of solution processing. Controlling the valence state of molybdenum (Mo) in MoO_x HTL is critical for OSCs performance. In this work, we developed a novel methode based on photochemical reduction to synthesize $HMoO_x$ nanoparticle ink for OSCs. $HMoO_3$ nanoparticle was firstly obtained through oxidaiton of metal molybdenum. Afterward, the $HMoO_3$ precursor nanoparticles were continuously illuminated to induce the reduction of Mo(VI) to Mo(V) to form $HMoO_x$. Such a process could proceed under the illumination of different light sources, even sunlight. In addition, photoelectron spectroscopy (XPS) and absorption spectra demonstrated such a photoreduction process was well controllable by illumination intensity and illumination time. With this $HMoO_x$ HTL for the inverted OSCs, a high efficiency of 13.17% and 16.64% for the PM7:IT-4F and PM6:Y6 OSCs was obtained, which is comparable with the evaporated MoO_3 HTL-based OSCs. Furthermore, based on the Ag nanowires (AgNWs) electrode, the performances of all-solution-processed PM6:Y6 semitransparent device also reach 10.52%. This work provides a simple and feasible route to fabricate hole transporting layer for solution-processable OSCs.

1. Introduction

Organic solar cells (OSCs) have attached extensive attention to the new generation photovoltaics due to their advantages of flexible, colourful, and roll-to-roll process-compatible [1–5]. With the development of organic semiconductor materials and interlayer engineering [6–10], the highest power conversion efficiency (PCE) of the OSCs has reached over 18% [11–14], demonstrating the excellent application prospect of OSCs in the future.

Compared to vacuum deposition conditions, the solution-process has the advantages of low cost, high yield and simple production equipment. To achieve the full-solution-processed fabrication of OSCs, solution-processed hole transporting layer (HTL) is critical. Molybdenum oxide (MoO_3) is a widely used HTL material in the OSCs [15,16]. However, the traditional MoO_3 HTL was prepared by thermal evaporation under high vacuum conditions [17–19], which would be a drawback regarding the full-solution-processed fabrication. Up to now, mainly three types of solution-processable MoO_x inks have been developed. First approach was hydrolysing of ammonium heptamolybdate tetrahydrate (NMo) to form MoO_x [20,21]. This method is simple, but the resulted MoO_3 layer has poor electrical conductivity. The second route was oxidation of metal Mo to form hydrogen molybdenum bronze $HMoO_x$ [22,23]. In such process, hydrogen peroxide (H_2O_2) is involved in the preparation, and the ratio of Mo(V)/Mo(VI) was difficult to be well controlled. The third route was using sol–gel precursor MoO_x inks to achieve the expected films [24,25]. In general, $Mo(CO)_3(EtCN)_3$, $MoO_2(acac)_2$, *etc.*, were used as the precursor salts, and the MoO_x layer was obtained through hydrolysing and aging. In this process, the precursor should be

* Corresponding authors at: School of Nano-Tech and Nano-Bionics, University of Science and Technology of China, Hefei 230026, PR China; Printable Electronics Research Center, Suzhou Institute of Nano-Tech and Nano-Bionics, Chinese Academy of Sciences(CAS), Suzhou 215123, PR China (Q. Luo and C.-Q. Ma).
E-mail addresses: qluo2011@sinano.ac.cn (Q. Luo), cqma2011@sinano.ac.cn (C.-Q. Ma).

https://doi.org/10.1016/j.cej.2021.130620
Received 18 March 2021; Received in revised form 16 May 2021; Accepted 28 May 2021
Available online 4 June 2021

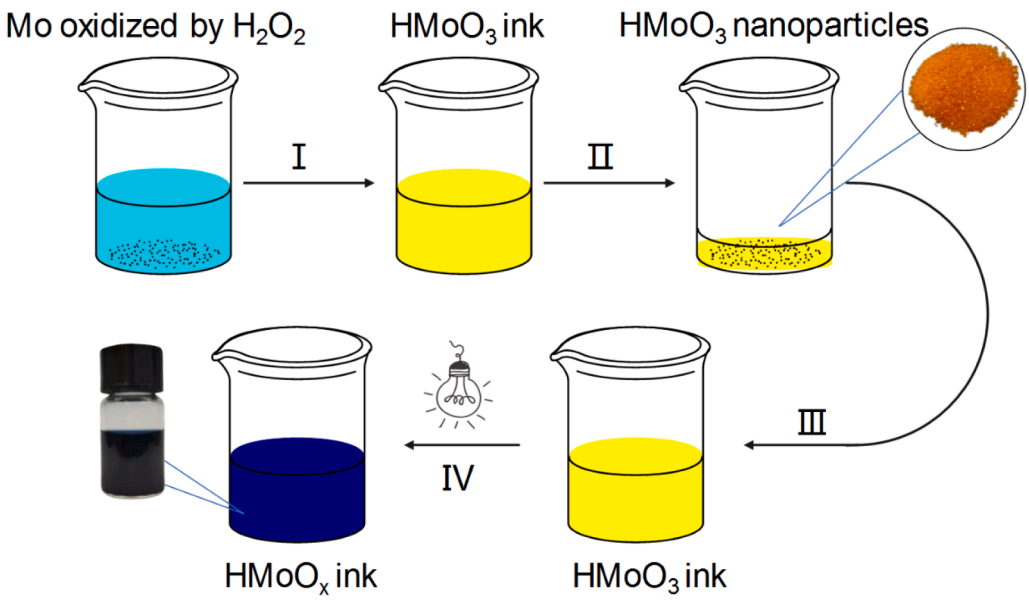

Scheme 1. The process diagram of $HMoO_x$ nanoparticle ink preparation. I: synthesis of $HMoO_3$ nanoparticles, II: dry and collection, III: re-dispersion the $HMoO_3$ in solvent, IV: photoreduction to form $HMoO_x$ inks.

maintained at ambient conditions for a couple of days, which is incompatible with scale-up technologies [26–28].

The previous works showed both the conductivity and work function of MoO_x is highly dependent on the composition [29,30]. Generally, MoO_x with a mixed valence of Mo(V) and Mo(IV) has increased conductivity compared to the pure MoO_3 with sole valence state of Mo(VI). Therefore, accuracy control of the composition of MoO_x is necessary. To achieve this, some reduction agents, ethylene glycol (EG), vitamin C (VC) were used to reduce Mo(VI) and form n-doping in the MoO_x films. Kang *et al.* utilized EG as a modifier of the MoO_3 film. Mo(V) generated in the MoO_3 film due to reduction of Mo(VI) by EG. The generation of Mo(V) in the MoO_3 films lead to highly conductive MoO_x:EG HTL. It enabled a high efficiency of 12.1%, which is comparable to that of the PEDOT:PSS HTL-based devices [20]. Analogously, Yang *et al.,* used VC as an additive to lead transforming of Mo(VI) to Mo(V) in the MoO_x ink, realizing a thickness insensitive MoO_x HTL [31]. These works developed a good n-doped MoO_x HTL through chemical reduction for OSCs.

MoO_x is typical transition metal oxide and has been used in surface-enhanced Raman scattering, electrochromic, photochromic *etc.* [32–34]. The photochromic process of MoO_x involved in the change of Mo chemical valence from Mo(VI) to Mo(V) under the irradiation of UV light. Homoplastically, based on photochromic properties of MoO_x, we adopted such a photo-reduction method to partially induce the transformation of $HMoO_3$ to $HMoO_x$ to achieve n-doping. The ratio of Mo(V) to Mo(VI) in the $HMoO_x$ nanoparticle inks was controlled by the illumination time and illumination intensity. A tight relationship between the ratio of Mo(V) to Mo(VI) and the absorption intensity in the visible-NIR region was established. This could be used as a simple criterion to evaluate the composition. Finally, based on the optimizing of $HMoO_x$ nanoparticle ink, a high efficiency of 13.17% and 16.64% for the PM7:IT-4F and PM6:Y6 heterojunction solar cells was achieved. Besides, the PCE of an all-solution-processed semi-transparent device with solution-processed MoO_x HTL and Ag nanowires (AgNWs) electrode reached 10.52%, showing an excellent application prospect. This work provides a simple and scalable method to synthesis $HMoO_x$ nanoparticles inks through controllable photo-reduction route.

2. Experimental section

2.1. Materials

Mo powders were purchased from Shanghai Aladdin Reagent Co. Ltd. PM7, PM6, IT-4F, and Y6 were purchased from solarmer Materials Inc, Beijing. The AgNWs were purchased from H&C Advanced Materials Ltd.

2.2. Synthesis of $HMoO_x$ inks

Firstly, the precursor $HMoO_3$ nanoparticle ink was prepared by 100 mg Mo powder and 1.5 mL 30% hydrogen peroxide (H_2O_2) solution, with 10 mL ethanol added as the solvent. After 30 min, the yellow $HMoO_3$ sol was collected by removing the solvent, and then redispersed in ethanol with a concentration of 10 mg/mL. Then, the $HMoO_3$ nanoparticle ink was illuminated under different LED lamp sources or sunlight, and a series of $HMoO_x$ nanoparticles were obtained. Two kinds of LED lamps were used in this work. One kind lamp was the desk LED lamp, which has low irradiation intensity around 6000 lx. The other lamp was LED array, which has strong irradiation intensity around 80,000 lx.

2.3. OSCs fabrication

Inverted OSCs with a structure of ITO/ZnO/active layer/$HMoO_x$/Al were fabricated according to the following procedure. Patterned ITO substrates were subsequently sonically cleaned in deionized water, acetone, and isopropanol, and finally treated in ultraviolet ozone (UVO) for 30 min. A 30 nm thick ZnO cathode buffer layer was deposited through spin-coating at 2000 rpm for 60 s and followed by thermal treating at 130 °C for 10 min in air. After that, the ITO/ZnO substrates were then transferred to a nitrogen-filled glove-box for the deposition of the photoactive layers. PM7 (10 mg) and IT-4F (10 mg) were dissolved in 1 mL chlorobenzene (Sigma-Aldrich) with 0.5 vol% of 1,8-diiodooctane (DIO, Sigma-Aldrich) and stirred at 45 °C for 5 h. Analogously, PM6 (7 mg) and Y6 (8.4 mg) were dissolved in 1 mL chloroform (Sigma-Aldrich) with 0.5 vol% of chloronaphthalene (CN, Sigma-Aldrich) and stirred at 45 °C for 3 h. The photoactive layer was deposited on the ZnO layer by spin-coating at 2000 rpm for 60 s and thermally annealed at 100 °C for 10 min in a nitrogen-filled glove box. The $HMoO_x$ layer was

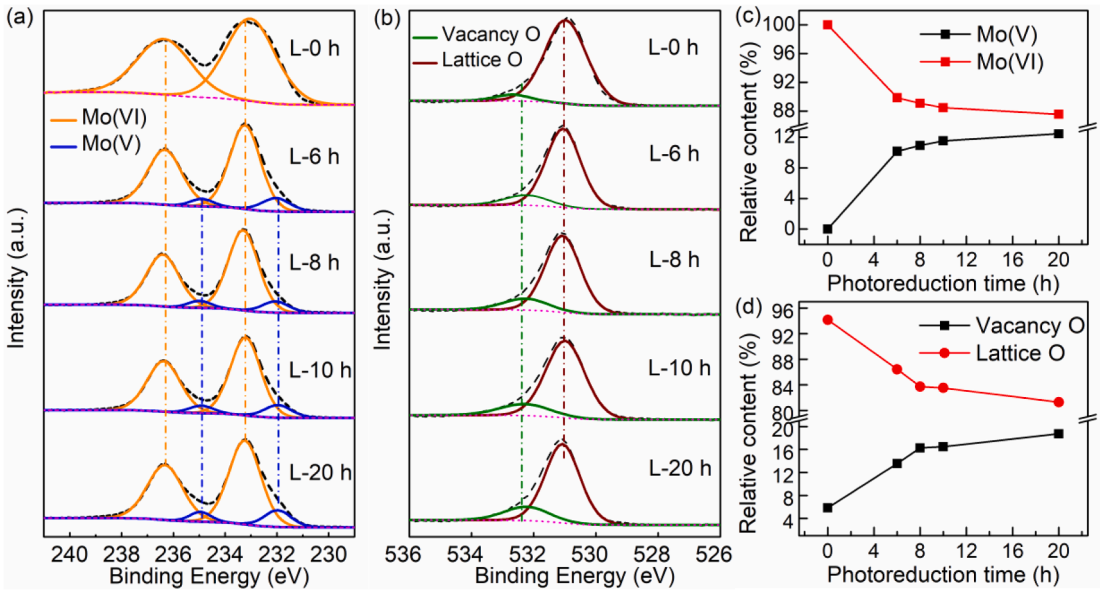

Fig. 1. (a) XPS spectra of Mo 3d and (b) XPS spectra of O 1 s of $HMoO_x$ nanoparticle inks; (c) Mo 3d and (d) O 1 s changing tendency with different photoreduction times.

spin-coated on the photoactive layer at 2000 rpm for 60 s from the $HMoO_x$ solution (10 mg/mL). Finally, 100 nm Al electrode was evaporated deposited at a vacuum degree of 4×10^{-4} Pa. Besides, for the all-solution-processed device, the AgNWs (2.5 mg/mL) were sprayed on the $HMoO_x$ HTL in air with a spray coater (Hizenith AC300-1, Hizenith Robot (Suzhou) Co. Ltd). The pressure of the carrier gas was 28 Pa, the nozzle moving speed was 16 mm/s, and the substrates were kept on the hotplate at 55 °C.

2.4. Characterization

The UV − vis absorption spectra of the $HMoO_x$ inks were recorded by the Lambda 750 UV/vis/NIR spectrophotometer (PerkinElmer). The ultraviolet photoelectron spectroscopy (UPS) and X-ray photoelectron spectroscopy (XPS) of the $HMoO_x$ films were recorded by the Kratos Asxis Ultra DLD (Kratos Analytical Shimadzu Group Company). An unfiltered He − I (21.2 eV) discharge lamp and a total instrumental energy resolution of 100 meV was used for UPS measurement. An Al Kα radiation source was used for the XPS measurement. The $J - V$ measurement was carried out with a Keithley 2400 source meter under simulated AM 1.5G solar illumination (100 mW/cm^2). EQE spectra were measured under simulated one sun operation conditions with light from a 150 W tungsten halogen lamp (Osram 64610) as the probe light, a monochromator (Zolix, Omni-λ300) for selecting the wavelength, and a *J–V* converter for recording the response. The light was illuminated on the sample *via* a small aperture with a radius of 1.5 mm. A calibrated Si cell was used as a reference, and the device was kept behind a quartz window in a nitrogen-filled container. The long-term stability of devices was conducted using a multichannel solar cell performance decay test system (PVLT-G8001M, Suzhou D&R Instruments Co. Ltd.)

3. Results and discussion

The synthesis process of $HMoO_x$ nanoparticle ink can be divided into four steps, as Scheme 1 shown. (I) The preparation of precursor $HMoO_3$ nanoparticle ink: The $HMoO_3$ nanoparticle ink was prepared through oxidation of the Mo power by H_2O_2 followed the similar method reported by Xie and Wang *et al.* with some modifications [35,36]. Herein, excess H_2O_2 was used to make sure the formation of $HMoO_3$ with sole Mo(VI). The detailed process could be read in the experimental section. The X-ray diffraction (XRD) patterns showed the $HMoO_3$ nanoparticles were amorphous (**Fig. S1**), and the thermogravimetry analysis (TGA) demonstrated that the $HMoO_3$ nanoparticles contain water, including the physically adsorbed water molecules (~100 °C) and structural water (~210 °C) (**Fig. S2**) [37]. Some previous reports have demonstrated the obtained nanoparticles were hydrogen molybdenum bronzes [35]. Therefore, the nanoparticles are named as $HMoO_3$. (II) The yellow $HMoO_3$ particles were collected by removing the solvent, washing, and drying in a vacuum. The obtained $HMoO_3$ nanoparticles could be stored in the glove box for future use. (III) The yellow $HMoO_3$ particles were redispersed in ethanol with a concentration of 10 mg/mL to form $HMoO_3$ nanoparticle ink. (IV) The $HMoO_3$ nanoparticleink was illuminated by different lamps under continuous stirring. During illumination, the yellow $HMoO_3$ inks gradually changed to green, blue, and dark blue, and the target $HMoO_x$ nanoparticle inks were obtained.

Firstly, a home-made LED array lamp with intensity of 80,000 lx was used to systematically study the photoreduction process. **Fig. S3** shows the irradiation spectrum of the lamp. This figure showed the lamp spectrum contained a narrow band from 400 to 500 nm and one wide peak from 500 to 800 nm. The XPS spectra were used to monitor the transformation process of $HMoO_3$ precursor. L-0 h, L-6 h, L-8 h, L-10 h, and L-20 h refer to $HMoO_x$ inks which were obtained by illuminating the $HMoO_3$ precursor inks for 0, 6, 8, 10, and 20 h, respectively. Fig. 1**(a)** shows the core level of Mo 3d of the $HMoO_x$ nanoparticle inks. The XPS spectrum of the L-0 h $HMoO_x$ ink displays two symmetric peaks at 232.8 and 235.9 eV, which were ascribed to Mo(VI) $3d_{5/2}$ and Mo(VI) $3d_{3/2}$ respectively[27,38,39]. After illumination for more than 6 h, besides the peaks at 232.8 and 235.9 eV from Mo(VI), doublet peaks at 234.9 and 231.8 eV ascribed to Mo(V) were also observed, demonstrating the occurrence of photoreduction from Mo(VI) to Mo(V) [40]. Fig. 1**(b)** shows the core level of O 1 s of the $HMoO_x$ nanoparticle inks. As we can see here, the XPS spectra for all the inks display two symmetric peaks at 531.0 and 532.4 eV, which were ascribed to lattice oxygen and vacancy oxygen of $HMoO_x$ respectively [24,41–43]. However, the ratio of vacancy oxygen in the HMoOx inks was higher than the pristine $HMoO_3$ ink. To clearly show this change, the percentage of Mo(V), Mo(VI) and the percentage of vacancy oxygen, lattice oxygen were calculated and showed in Fig. 1**(c) and (d).** Obviously, the ratio of Mo(V) gradually increased from 0 to 12.4%, while the ratio of Mo(VI) decreased from 100% to 87.6%. Correspondingly, the vacancy oxygen is growing as the increasing in the photoreduction time.

In the foregoing process, we demonstrated that light irradiation of

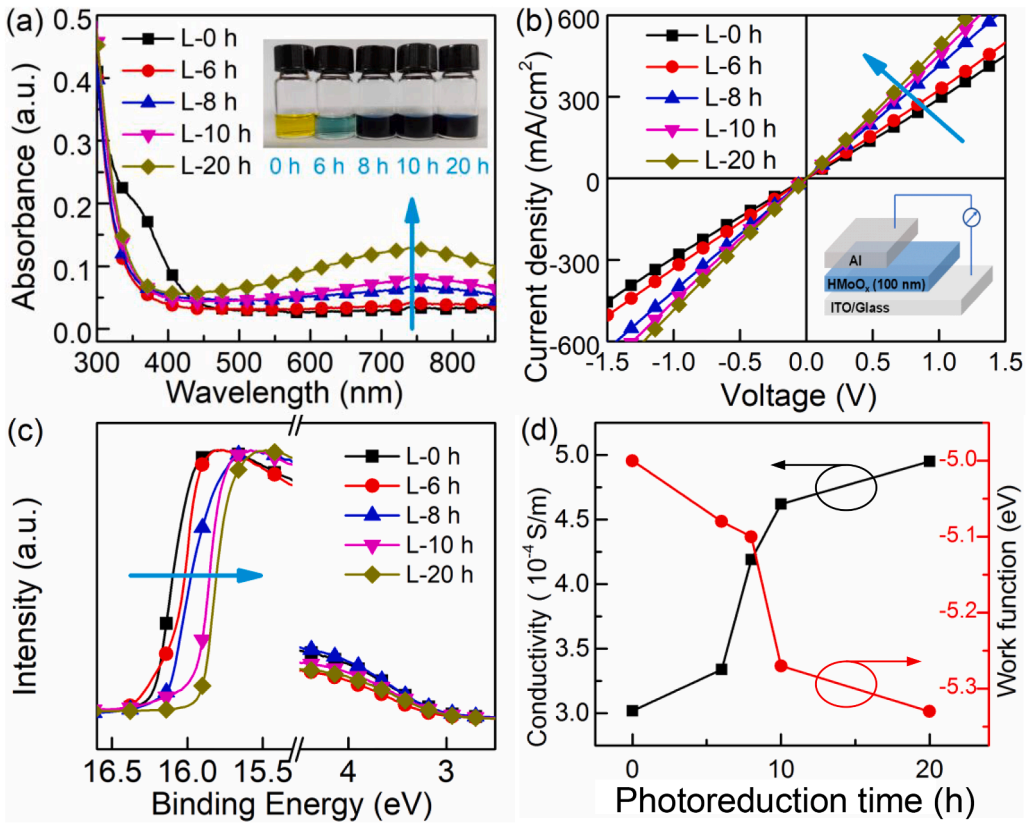

Fig. 2. (a) UV–vis absorption spectra of the $HMoO_x$ nanoparticle inks, and the inset shows the photographic picture, (b) *J–V* curves of the devices, and the inset is the device structure, (c) UPS spectra of the $HMoO_x$ films, (d) The changing tendency of work function and conductivity of the $HMoO_x$ films.

the $HMoO_3$ precursor ink can lead to the increasing of vacancy oxygen, and reduce the content of Mo(VI). Meanwhile, the property of $HMoO_x$ ink changed with the illuminated time. Fig. 2**(a)** shows the photograph and the UV–vis absorption spectra of the $HMoO_x$ nanoparticle inks. As we can see here, the L-0 h $HMoO_3$ ink only shows an absorption band at around 350 nm, which is the typical absorption band of MoO_3. While almost no absorption in the range from 500 to 860 nm was observed, indicating the obtained $HMoO_3$ inks might be pure $HMoO_3$ without impurities. That's reasonable since excess H_2O_2 was added in the first reaction step. But for the inks, a strong absorbance peak at 600 ~ 800 nm can be observed. Besides, with the illumination time gradually increases to 20 h, the absorption intensity of the $HMoO_x$ inks in the wavelength region (600 ~ 800 nm) is regularly enhanced. Correspondingly, the photograph of the $HMoO_x$ inks showed that the color of inks gradually turned from yellow (L-0 h $HMoO_3$ ink) to light green (L-6 h $HMoO_x$ ink) and finally turned to dark blue (L-8 h, L-10 h, and L-20 h $HMoO_x$ ink). In contrast, as **Fig. S4** shown, the $HMoO_3$ nanoparticle ink kept yellow when be stored in a dark environment for 20 h, and the absorption spectra also nearly showed no change when stored in dark. Therefore, this result proved the transformation from Mo(VI) to Mo(V) was mainly accelerated by light illumination. Also, a similar transformation was observed as the $HMoO_x$ nanoparticle were dispersed in water, methanol, ethanol, and IPA (as **Fig. S5** shown).

Fig. 2**(b)** shows the conductivity of the 100 nm thick $HMoO_x$ films as a function of illumination time, which was estimated by measuring the *J–V* curves of the devices with the structure of ITO/$HMoO_x$/Al[44,45]. As we can see, all the devices show a linear *J–V* relation. The calculated data are listed in Table S1. The $HMoO_3$ (L-0 h) film has the lowest

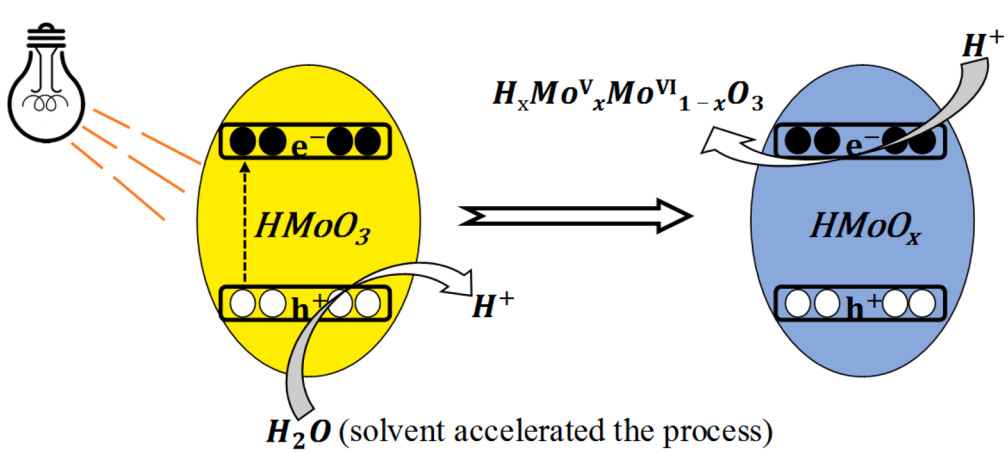

Fig. 3. The diagram of mechanism for $HMoO_3$ inks under illumination.

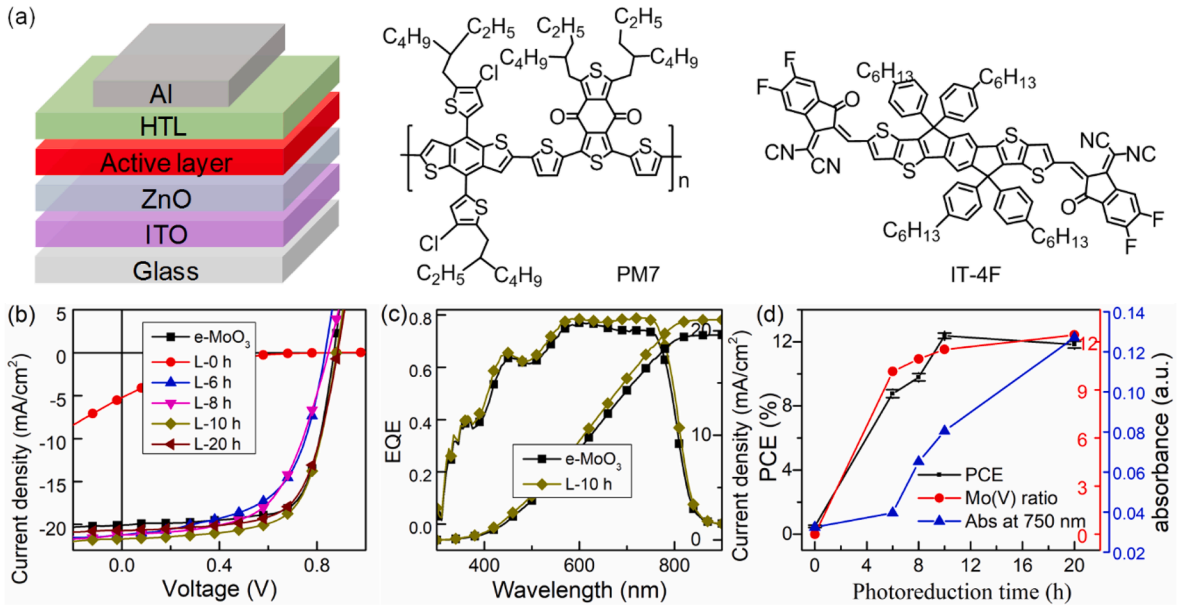

Fig.4. (a) Device structure and molecular structure of PM7, IT-4F, (b) $J-V$ curves and (c) EQE spectra of the PM7:IT-4F devices, (d) the evolution of Mo(V) ratio, absorption intensity at 750 nm, and device performance during the increase of photoreduction time.

conductivity of 3.02×10^{-4} S/m. After white light illumination, the conductivity of the $HMoO_x$ layer is enhanced gradually. When the time increased to 20 h, the conductivity of the $HMoO_x$ layer reached the highest value of 4.95×10^{-4} S/m, which is ascribed to an enhanced n-doping effect. In a word, the conductivity of the $HMoO_x$ films can be well controlled by illumination time. Meanwhile, the work function of the series of $HMoO_x$ films was characterized by ultraviolet photoelectron spectroscopy (UPS). As shown in Fig. 2**(c)**, with the increasing illumination time, the work function of the $HMoO_x$ layers increased gradually. From L-0 h to L-20 h $HMoO_x$ inks, the work function was − 5.00, −5.08, −5.10, −5.27, and − 5.33 eV, respectively. Such composition-dependent work function of $HMoO_x$ has been reported previously [23,46]. The increased work function is in favour of level matching between donor and electrode in OSCs. Besides, Fig. 2**(d)** illustrated the variation tendency of the conductivity and work function. The increased conductivity and work function of the $HMoO_x$ HTL are favourable to the OSCs performance.

The XPS results, combing the absorption spectra of these $HMoO_x$ proved the transformation from $HMoO_3$ to $HMoO_x$ is a typical photochromic phenomenon of Mo(VI), and the similar mechanism has been reported in MoO_3 and WO_3 previously[47–50]. The detail process could be described as follow (as Fig. 3 shown): under light illumination, $HMoO_3$ (Mo(VI)) can be excited and generate electrons and holes [48]. The photo generated electron would be injected into the conduction band and caused the reduction from Mo(VI) to Mo(V). The generated holes would be trapped by the adsorbed water to generate protons. But, since the adsorbed water would be nearly negligible in the dried powers, herein the dried $HMoO_3$ powers were relative stable, especially as it was stored in the glove box. As the nanoparticles were redispersed in solvent. The existence of solvents, *i.e.,* water, methanol, ethanol, IPA, and n-butanol can accelerate the reduction through provide protons and injection protons into the system in such a process[48,51]. The protons diffuse into the lattice, and the photogenerated electrons injected into the conduction band of $HMoO_3$ and reacted with $HMoO_3$ to form the blue-coloured hydrogen molybdenum bronze ($H_xMo_x^{V}Mo_{1-x}^{VI}O_3$) with Mo (V) [52].

To check the function of $HMoO_x$ nanoparticle inks as HTL, inverted OSCs with the structure of ITO/ZnO/active layer/HTL/Al (as shown in Fig. 4**(a)**) were fabricated. The pristine $HMoO_3$ and photo-reduced $HMoO_x$ HTLs were fabricated and deposited on the top of the photoactive layer. The molecular structure of organic donor and acceptor are showed in Fig. 4**(a)**. Firstly, PM7:IT-4F heterojunction solar cells were fabricated, and $HMoO_x$ HTLs fabricated from different photoreduction time were used. Fig. 4**(b)** shows the *J-V* curves of the OSCs with different $HMoO_x$ HTLs, and the statistical photovoltaic performance data are listed in Table 1. As seen here, the device with L-0 h $HMoO_x$ HTL showed a minimal power conversion efficiency (PCE) of 0.59%, with the lowest short circuit current (J_{SC}) of 5.23 mA/cm^2 and fill factor (FF) of 0.14. With the increasing of illumination time, the PCE of OSCs boosted to 9.28% for the L-6 h $HMoO_x$ HTL-based device, and synchronous increase of J_{SC} (21.22 mA/cm^2) and FF (0.54) were observed. This result was in good agreement with the previous report that the existence of Mo(V) can improve the $HMoO_x$ HTL performance [31]. Besides, L-8 h $HMoO_x$-based OSCs showed a slight higher performance of 10.22% compared to the L-6 h $HMoO_x$-based device. Notably, a high PCE of 13.17% was obtained from the device of L-10 h $HMoO_x$

Table 1
Photovoltaic properties of the inverted OSCs with $HMoO_x$ and e-MoO_3 HTLs.

Active layer	HTL	V_{OC} (V)	J_{SC} (mA/cm^2)	Integrated J_{SC} (mA/cm^2)	FF	PCE max (%)	PCE ave. (%)[a]
PM7:IT-4F	e-MoO_3	0.87 ± 0.01	20.28 ± 0.13	19.58	0.71 ± 0.01	12.79	12.54 ± 0.19
	L-0 h	0.81 ± 0.00	4.67 ± 0.56	5.20	0.13 ± 0.01	0.59	0.57 ± 0.07
	L-6 h	0.81 ± 0.00	21.02 ± 0.20	20.58	0.52 ± 0.02	9.28	9.01 ± 0.25
	L-8 h	0.85 ± 0.01	21.01 ± 0.19	20.60	0.55 ± 0.01	10.22	9.99 ± 0.23
	L-10 h	0.88 ± 0.00	21.43 ± 0.26	21.04	0.68 ± 0.01	13.17	12.97 ± 0.17
	L-20 h	0.87 ± 0.01	21.23 ± 0.12	20.73	0.66 ± 0.01	12.60	12.32 ± 0.21

[a]PCE_{ave} was calculated over more than 12 individual devices, and the device area is 0.09 cm^2.

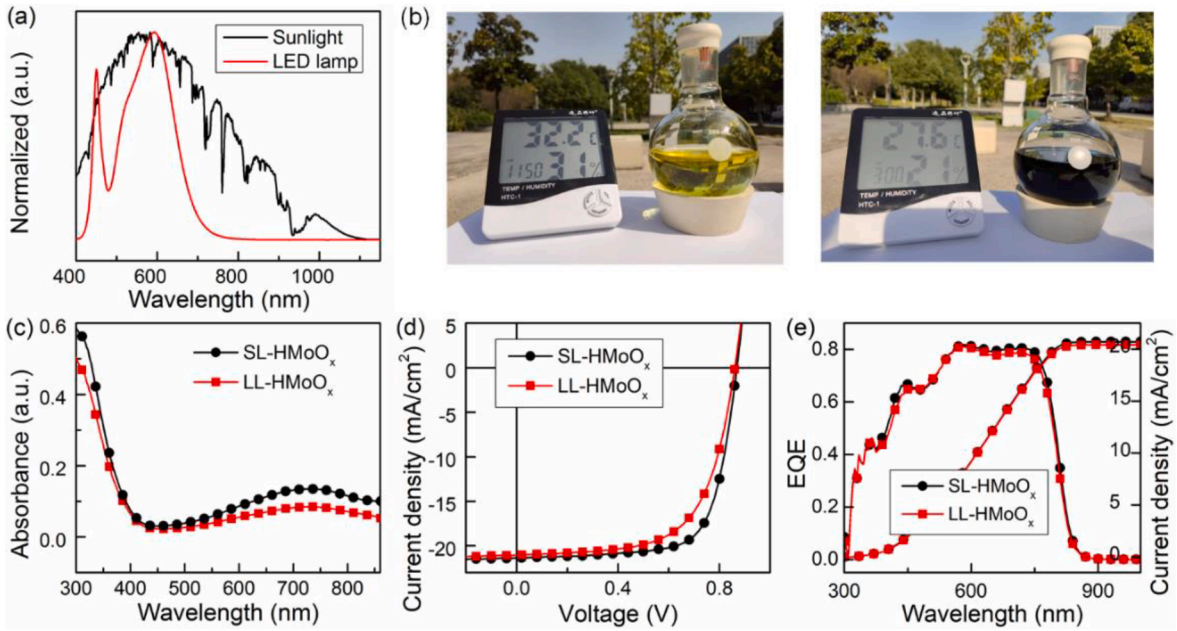

Fig.5. (a) The normalized absorption spectrum of the sunlight and LED lamp, (b) the photograph of the $HMoO_3$ ink under irradiation of sunlight, (c) UV–vis absorption spectra of the SL-$HMoO_x$ and LL-$HMoO_x$ nanoparticle inks, $J - V$ curves (d), and EQE spectra (e) of OSCs with two kinds of $HMoO_x$ inks.

HTL, with a J_{SC} of 21.69 mA/cm^2, a V_{OC} of 0.88 V, and an FF of 0.69. Such performance was even superior to the device with evaporation-processed MoO_3 (e-MoO_3) HTL (PCE, 12.79%), demonstrating the outstanding hole transporting ability of L-10 h $HMoO_x$ HTL. In other words, the $HMoO_x$ prepared from photoreduction could be utilized in OSCs as a replacement of the e-MoO_3 HTL with comparable performance. Further prolonging the illumination time, the performance of L-20 h $HMoO_x$-based OSCs is slightly inferior to the L-10 h $HMoO_x$ device. A PCE of 12.60% with a slight reduction in J_{SC} and FF (21.35 mA/cm^2, 0.67) was observed. But such performance was still comparable with e-MoO_3-based solar cells. This result demonstrated the composition of $HMoO_x$ highly influenced the device performance of the OSCs. Benefiting from the time-dependent composition of the $HMoO_x$ films, it is relatively easy to obtain proper $HMoO_x$ inks by the photoreduction route. Besides, the illumination time has a wide range of operation windows (from 10 h to 20 h), which is benefit for the production of $HMoO_x$ nanoparticle ink. Fig. 4**(c)** was the EQE spectra and the integrated current of the optimized devices. The e-MoO_3 HTL and $HMoO_x$ HT-based devices showed an integrated current of 19.58 and 21.04 mA/cm^2, respectively. These integrated currents were in good agreement with the J_{SC} from J-V curves.

Based on the foregoing research results, the relation of the device performance with the absorption intensity at 750 nm and the ratio of Mo (V) was exhibited as Fig. 4**(d)**. Herein, we found the device performance, the ratio of Mo(V), and the absorption intensity at 750 nm showed a similar trend with illumination time. Since the absorption spectrum of the nano-inks is a regular and easy measurement, such a variation trend implied the intensity of $HMoO_x$ ink absorption could be a quantitative criterion for the $HMoO_x$ ink photoelectric property during the preparation. Based on the relationship between the absorption spectra of $HMoO_x$ and the device performance (*vide supra*), we know when the peak intensity of $HMoO_x$ ink (0.01 mg/mL, ethanol) at 750 nm was equal to or higher than 0.08, the solution-processed $HMoO_x$ HTL would have a suitable ratio of Mo(V) in the inks.

Since we can evaluate the composition of the photo-reduced $HMoO_x$ inks using the absorption spectra, it would be possible to use different light sources to carry out the photoreduction experiment. Therefore, we tried to illuminate the $HMoO_3$ inks using sunlight and other LED lamps. We found the reduction from Mo (VI) to (V) can be successfully achieved by using these two light sources, which provide available options for $HMoO_x$ ink preparation. Fig. 5**(a)** exhibits the normalized spectra of the desk LED lamp and sunlight, and Fig. 5**(b)** shows the variation of $HMoO_3$ ink change to $HMoO_x$ ink under sunlight. Herein, the desk LED lamp has a weak intensity of 6000 lx. Fig. 5**(c)** shows the UV–vis absorption spectra of the obtained $HMoO_x$ inks, which were illuminated under an LED lamp for 240 h (named as LL-$HMoO_x$) and under sunlight for 3 h

Table 2
Photovoltaic performance of the PM7:IT-4F and PM6:Y6 solar cells with $HMoO_x$ HTLs.

Materials	HTL	V_{OC} (V)	J_{SC} (mA/cm^2)	Integrated J_{SC} (mA/cm^2)	FF	PCE_{max} (%)	PCE [a)] $_{ave.}$ (%)
PM7:IT-4F	SL-$HMoO_x$	0.88 ± 0.00	21.22 ± 0.14	20.71	0.70 ± 0.01	13.34	12.95 ± 0.09
	LL-$HMoO_x$	0.86 ± 0.01	20.87 ± 0.17	20.41	0.67 ± 0.01	12.45	12.11 ± 0.21
PM6:Y6	e-MoO_3	0.84 ± 0.00	26.77 ± 0.12	26.06	0.73 ± 0.00	16.48	16.22 ± 0.09
	SC-$HMoO_x$	0.84 ± 0.00	27.21 ± 0.19	26.59	0.72 ± 0.00	16.58	16.38 ± 0.12
	DBC-$HMoO_x$	0.84 ± 0.01	27.01 ± 0.18	26.63	0.71 ± 0.01	16.64	16.44 ± 0.25
	SL-$HMoO_x$ [b)]	0.82 ± 0.01	18.19 ± 0.45	18.07	0.66 ± 0.02	10.52	10.04 ± 0.43

SL-$HMoO_x$, LL-$HMoO_x$ stands for the $HMoO_x$ illuminated under solar light and LED table lamp. SC-$HMoO_x$, DBC-$HMoO_x$ stand for the spin-coated, and doctor-blade-coated $HMoO_x$ HTLs.

[a)] PCE_{ave} was calculated over more than 12 individual devices, and the area of the PM7:IT-4F device was 0.09 cm^2, and the area of the PM6:Y6 device was 0.04 cm^2.

[b)] This device was a semitransparent device.

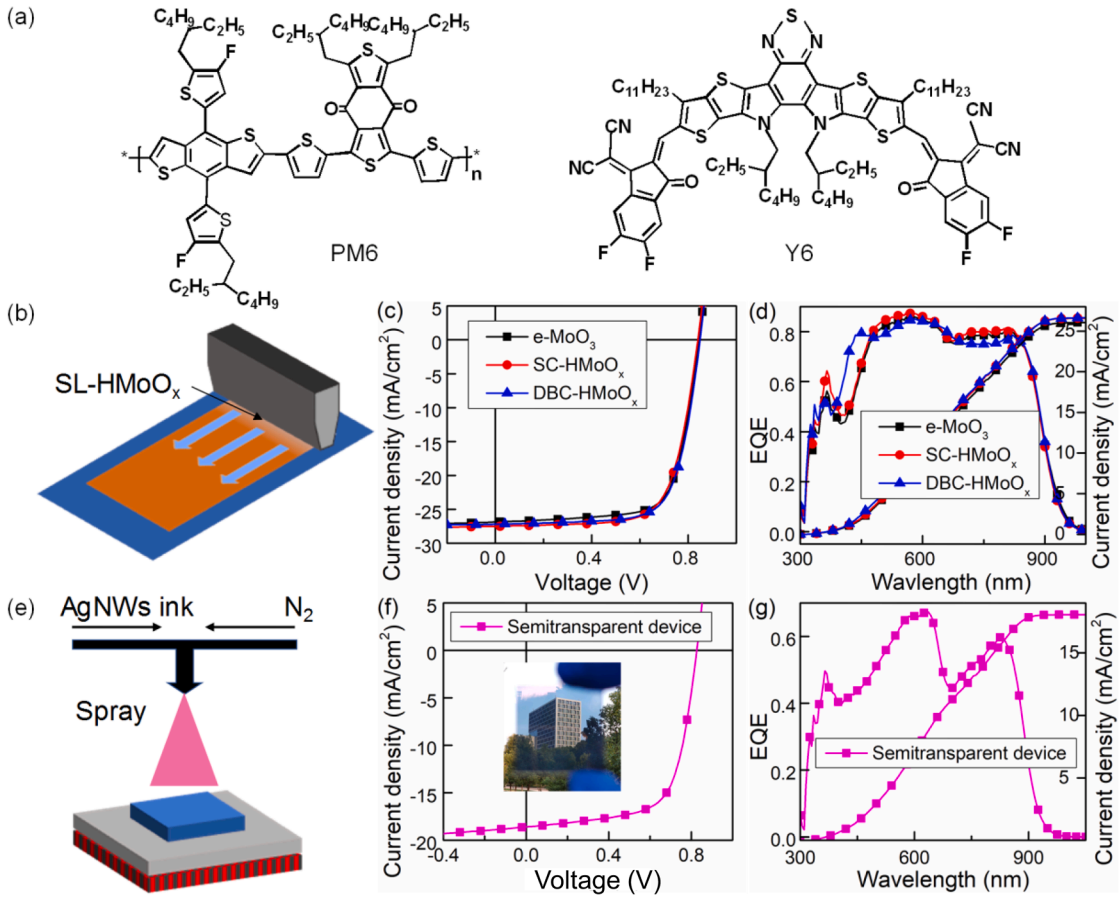

Fig.6. (a) The molecular structure of PM6 and Y6, (b) The diagram of doctor-blade-coating of the $HMoO_x$ HTL, (c) *J-V* curves and (d) EQE spectra of the PM6:Y6 solar cells with e-MoO_3, SC-$HMoO_x$, and DBC-$HMoO_x$ HTL, (e) The diagram of spray-coating of the AgNWs electrode, (f) *J-V* curves and (g) EQE spectra of the semitransparent device with DBC-$HMoO_x$ HTL and spray-coated AgNWs electrode.

(named as SL-$HMoO_x$). For two light sources used for $HMoO_x$ nanoparticle ink preparation, the illumination time were different due to different illumination intensity and light spectra. On the side of illumination intensity, as Fig. 3**(a)** shown, we see the LED array lamp with intensity of 80,000 lx took around 8–10 h to achieve the target $HMoO_x$ nano inks, while the desk LED lamp took 240 h (as showed by **Fig. S6**). On the side of illumination spectrum, since the cut-off of the absorption spectrum of $HMoO_3$ is about 450 nm, we mainly focused on the influence of vis-blue wavelength region. Here, light with wavelength from 400 to 600 and from 600 to 800 nm was compared. **Fig. S7** shows the absorption change of the $HMoO_x$ inks. It showed that nearly no change was observed using light with wavelength of 600–800 nm. It indicated the light spectrum should include vis-blue short wavelength region.

Under the illumination of the desk LED lamps and sunlight, the absorption intensity of the obtained $HMoO_x$ inks (0.01 mg/mL) at 750 nm was 0.13 and 0.09, higher than the lowest value of 0.08. It indicated the inks could satisfy the usage requirement of solution-processed $HMoO_x$ for OSCs. Fig. 5**(d, e)** show the *J-V* and EQE curves of the device with different $HMoO_x$ inks, and the statistical photovoltaic performance data are listed in Table 2. As seen here, the devices based on SL-$HMoO_x$/LL-$HMoO_x$ ink show the similar performance of 13.34% and 12.45%, demonstrating the universality of different light sources for $HMoO_x$ nanoparticle preparation. These results showed the great advantage of this photo-reduction synthesis method, especially utilizing the sunlight can be an environmental-friendly and economical way. From the EQE spectra of the devices, the integrated current was 20.71 and 20.41 mA/cm^2 for the SL-$HMoO_x$ and LL-$HMoO_x$ devices.

Furthermore, we demonstrated the universal application of the $HMoO_x$ nanoparticle ink in different active layers-based OSCs and different processing methods. First, to show the generality of the $HMoO_x$ inks for OSCs, PM6:Y6 bulk heterojunction was selected due to its high efficiencies [53,54], and SL-$HMoO_x$ ink was selected as an example. Fig. 6 **(a)** showed the molecular structure of PM6 and Y6. Fig. 6**(b)** shows the schematic diagram of the doctor-blade coating of $HMoO_x$ HTL with SL-$HMoO_x$ ink. Fig. 6**(c, d)** shows the *J-V* and EQE curves of the OSCs with different $HMoO_x$ HTL processing methods, and the statistical photovoltaic performance data are listed in Table 2. As seen here, a high PCE of 16.58% was obtained for the device with spin-coated $HMoO_x$ (SC-$HMoO_x$) HTL, which was comparable to the device with e-MoO_3 HTL (16.48%). Meanwhile, the device based on doctor-blade coated $HMoO_x$ (DBC-$HMoO_x$) HTL achieved a PCE of 16.64%. The optimized thickness of the $HMoO_x$ was around 15 nm, which is nearly the same as the thickness of e-MoO_3 HTL. The integrated current of the PM6:Y6 devices with e-MoO_3, SC-$HMoO_x$, DBC-$HMoO_x$ were 26.06, 26.59, and 26.63 mA/cm^2, respectively, which were similar to the values from *J-V* curves. After the successful application of these solution-processed $HMoO_x$ HTL in the OSCs, full-solution processable OSCs were fabricated based on spray-coated Ag nanowires (AgNWs) electrode, as Fig. 6 **(e)** shown. Fig. 6**(f, g)** showed the *J-V* and EQE curves of the OSCs, and the statistical photovoltaic performance data are listed in Table 2. As seen here, the all-solution-processed semitransparent device realized a PCE of 10.52%, a J_{SC} of 18.64 mA/cm^2, a V_{OC} of 0.83 V, and an FF of 0.68. Besides, as **Fig. S8** shown, the average transmittance of the OSCs over 300 ~ 1200 nm was 22.6%. From the above results, we see the $HMoO_x$ nanoparticle ink from the photoreduction route has excellent photoelectric property, making it a promising candidate of HTL in large-area roll-to-roll production.

As above mentioned, the ratio of Mo(V) to Mo(VI) in the $HMoO_x$

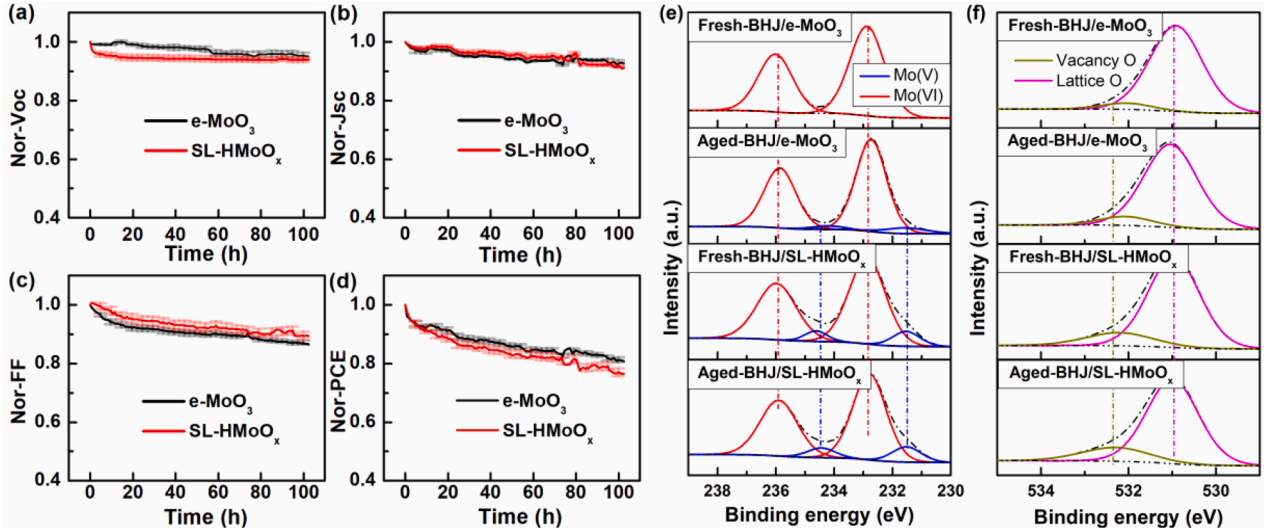

Fig. 7. (a-d) The evolution of the performance parameter of the e-MoO_3 and SL-$HMoO_x$ HTL-based organic solar cells during continuous illumination. (e) Mo 3d core level and (f) O 1 s core level of the BHJ/e-MoO_3 and BHJ/SL-$HMoO_x$ films before and after aging.

nano inks was well controlled by the light spectrum, illumination intensity, and the illumination time. Such as light-sensitivity of the $HMoO_x$ nano inks might be unfavoured for the device stability. Thus, the device stability of the OSCs based on PM6:Y6 materials system with the SL-$HMoO_x$ HTL was investigated. Fig. 7**(a-d)** shows the evolution of the performance data during continuous illumination in the glove box. The conventional e-MoO_3 and the solution-processed SL-$HMoO_x$ HTLs were used and compared. As showed by this figure, we observed a slight quicker degradation trend for the devices with $HMoO_x$ HTLs. In detail, after continuous illumination for 100 h, 84% and 78% of the initial efficiency was remained for the e-MoO_3 and SL-$HMoO_x$ devices. We also studied the XPS spectra of the fresh and aged devices. The XPS of the Mo 3d and O 1 s core levels (Fig. 7**(e) and (f)**) showed both the SL-$HMoO_x$ and e-MoO_3 showed composition change during continuous illumination. As listed in Table S2, the ratio of Mo(V) in the e-MoO_3 device increased from 0 to 6.87%, and correspondingly the ratio of oxygen vacancy to the lattice oxygen increased from 6.32% to 9.67% as well. For the devices with the $HMoO_x$ HTL, the aged films showed as increased Mo(V) content of 12.59% than that of the fresh device (10.72%). These results indicated in the SL-$HMoO_x$ and e-MoO_3 HTL-based devices, interface degradation at the interface of the active layer and HTL occurred, which might be due to photoreduction of molybdenum oxide and photooxidation of the active layer [55]. But the similar degradation speed implied the SL-$HMoO_x$ HTL could ensure a comparable stability as the e-MoO_3 devices.

4. Conclusion

In summary, we put forward a photochemical method to fabricate $HMoO_x$ nanoparticle ink and revealed the influence of light illumination condition on the composition and photoelectronic properties of the $HMoO_x$ HTLs. Specifically, light illumination induced the transforming of Mo(VI) to Mo(V) and form n-doping in the nanoparticles, leading to the increase of the conductivity and work function of the $HMoO_x$ films. Besides, the ratio of Mo(V) to Mo(VI) in the inks was controlled by the illumination time and illumination intensity. Using the photo-reduced $HMoO_x$ nanoparticle ink, a high efficiency of 13.17% and 16.64% for the PM7:IT-4F and PM6:Y6 OSCs was achieved. Besides, a high PCE of 10.52% for all-solution-processed PM6:Y6 semitransparent OSCs was obtained. This work provides a simple and mass-production comparable route to synthesize the solution-processed HTL.

Declaration of Competing Interest

The authors declare that they have no known competing financial interests or personal relationships that could have appeared to influence the work reported in this paper.

Acknowledgments

The work is financially supported by the National Natural Science Foundation of China (51773224), Youth Innovation Promotion Association, CAS (2019317), the Ministry of Science and Technology of China (2016 YFA0200700), and Vacuum Interconnected Nanotech Workstation, Suzhou Institute of Nano-Tech and Nano-Bionics, Chinese Academy of Sciences (CAS).

Appendix A. Supplementary data

Supplementary data to this article can be found online at https://doi.org/10.1016/j.cej.2021.130620.

References

[1] A. Karki, J. Vollbrecht, A.L. Dixon, N. Schopp, M. Schrock, G.N.M. Reddy, T.-Q. Nguyen, Understanding the high performance of over 15% efficiency in single-junction bulk heterojunction organic solar cells, Adv. Mater. 31 (48) (2019) 1903868, https://doi.org/10.1002/adma.v31.4810.1002/adma.201903868.

[2] Y. Han, X. Chen, J. Wei, G. Ji, C. Wang, W. Zhao, J. Lai, W. Zha, Z. Li, L. Yan, H. Gu, Q. Luo, Q.i. Chen, L. Chen, J. Hou, W. Su, C.-Q. Ma, Efficiency above 12% for 1 cm^2 flexible organic solar cells with Ag/Cu grid transparent conducting electrode, Adv. Sci. 6 (22) (2019) 1901490, https://doi.org/10.1002/advs.v6.2210.1002/advs.201901490.

[3] C. Zhang, Q. Luo, H. Wu, H. Li, J. Lai, G. Ji, L. Yan, X. Wang, D. Zhang, J. Lin, L. Chen, J. Yang, C. Ma, Roll-to-roll micro-gravure printed large-area zinc oxide thin film as the electron transport layer for solution-processed polymer solar cells, Org. Electron. 45 (2017) 190–197, https://doi.org/10.1016/j.orgel.2017.03.015.

[4] P. Bi, X. Hao, Versatile ternary approach for novel organic solar cells: A review, Sol. RRL 3 (1) (2019) 1800263, https://doi.org/10.1002/solr.v3.110.1002/solr.201800263.

[5] T. Yan, W. Song, J. Huang, R. Peng, L. Huang, Z. Ge, 16.67% rigid and 14.06% flexible organic solar cells enabled by ternary heterojunction strategy, Adv. Mater. 31 (39) (2019) 1902210, https://doi.org/10.1002/adma.v31.3910.1002/adma.201902210.

[6] W. Gao, T. Liu, C. Zhong, G. Zhang, Y. Zhang, R. Ming, L. Zhang, J. Xin, K. Wu, Y. Guo, W. Ma, H.e. Yan, Y. Liu, C. Yang, Asymmetrical small molecule acceptor enabling nonfullerene polymer solar cell with fill factor approaching 79%, ACS Energy Lett. 3 (7) (2018) 1760–1768, https://doi.org/10.1021/acsenergylett.8b0082510.1021/acsenergylett.8b00825.s001.

[7] P. Cheng, J. Wang, Q. Zhang, W. Huang, J. Zhu, R. Wang, S.-Y. Chang, P. Sun, L. Meng, H. Zhao, H.-W. Cheng, T. Huang, Y. Liu, C. Wang, C. Zhu, W. You,

X. Zhan, Y. Yang, Unique energy alignments of a ternary material system toward high-performance organic photovoltaics, Adv. Mater. 30 (28) (2018) 1801501, https://doi.org/10.1002/adma.v30.2810.1002/adma.201801501.

[8] Y. Lin, B. Adilbekova, Y. Firdaus, E. Yengel, H. Faber, M. Sajjad, X. Zheng, E. Yarali, A. Seitkhan, O.M. Bakr, A. El-Labban, U. Schwingenschlögl, V. Tung, I. McCulloch, F. Laquai, T.D. Anthopoulos, 17% efficient organic solar cells based on liquid exfoliated WS_2 as a replacement for PEDOT:PSS, Adv. Mater. 31 (46) (2019) 1902965, https://doi.org/10.1002/adma.v31.4610.1002/adma.201902965.

[9] J. Wei, G. Ji, C. Zhang, L. Yan, Q. Luo, C. Wang, Q.i. Chen, J. Yang, L. Chen, C.-Q. Ma, Silane-capped ZnO nanoparticles for use as the electron transport layer in inverted organic solar cells, ACS Nano 12 (6) (2018) 5518–5529, https://doi.org/10.1021/acsnano.8b0117810.1021/acsnano.8b01178.s001.

[10] G. Ji, W. Zhao, J. Wei, L. Yan, Y. Han, Q. Luo, S. Yang, J. Hou, C.-Q. Ma, 12.88% efficiency in doctor-blade coated organic solar cells through optimizing the surface morphology of a ZnO cathode buffer layer, J. Mater. Chem. A 7(1) (2019) 212-220. https://doi.org/10.1039/C8TA08873J.

[11] Q. Liu, Y. Jiang, K. Jin, J. Qin, J. Xu, W. Li, J. Xiong, J. Liu, Z. Xiao, K. Sun, S. Yang, X. Zhang, L. Ding, 18% efficiency organic solar cells, Sci. Bull. 65 (4) (2020) 272–275, https://doi.org/10.1016/j.scib.2020.01.001.

[12] J. Qin, L. Zhang, C. Zuo, Z. Xiao, Y. Yuan, S. Yang, F. Hao, M. Cheng, K. Sun, Q. Bao, Z. Bin, Z. Jin, L. Ding, A chlorinated copolymer donor demonstrates a 18.13% power conversion efficiency, J. Semicond. 42 (1) (2021) 010501, https://doi.org/10.1088/1674-4926/42/1/010501.

[13] J. Ke, X. Zuo, L. Ding, 18.69% PCE from organic solar cells, J. Semicond. 42 (6) (2021), 060502, https://doi.org/10.1088/1674-4926/42/6/060502.

[14] Y. Lin, M.I. Nugraha, Y. Firdaus, A.D. Scaccabarozzi, F. Aniés, A.-H. Emwas, E. Yengel, X. Zheng, J. Liu, W. Wahyudi, E. Yarali, H. Faber, O.M. Bakr, L. Tsetseris, M. Heeney, T.D. Anthopoulos, A simple n-dopant derived from diquat boosts the efficiency of organic solar cells to 18.3%, ACS Energy Lett. 5(12) (2020) 3663-3671. https://doi.org/10.1021/acsenergylett.0c01949.

[15] Q. Kang, Q. Liao, Y. Xu, L. Xu, Y. Zu, S. Li, B. Xu, J. Hou, P-doped conducting polyelectrolyte as anode interlayer enables high efficiency for 1 cm^2 printed organic solar cells, ACS Appl. Mater. Interfaces 11 (22) (2019) 20205–20213, https://doi.org/10.1021/acsami.9b04211.

[16] A.E.X. Gavim, M.R.P. da Cunha, E.R. Spada, T.N. Machado, F.S. Hadano, A. Ginane Bezerra, W. Herwig Schreiner, P.C. Rodrigues, A. Rashid bin Mohd Yusoff, A. G. Macedo, R.M. Faria, W.J. da Silva, Water-suspended MoO_3 nanoparticles prepared by lasis and fast processing as thin film by ultrasonic spray deposition, Sol. Energy Mater. Sol. Cells 200 (2019) 109986, https://doi.org/10.1016/j.solmat.2019.109986.

[17] X. Che, C.-L. Chung, C.-C. Hsu, F. Liu, K.-T. Wong, S.R. Forrest, Donor-acceptor-acceptor's molecules for vacuum-deposited organic photovoltaics with efficiency exceeding 9%, Adv. Energy Mater. 8 (19) (2018) 1703603, https://doi.org/10.1002/aenm.201703603.

[18] G. Wang, M.A. Adil, J. Zhang, Z. Wei, Large-area organic solar cells: Material requirements, modular designs, and printing methods, Adv. Mater. 31 (45) (2019) 1805089, https://doi.org/10.1002/adma.v31.4510.1002/adma.201805089.

[19] Y. Cui, H. Yao, L. Hong, T. Zhang, Y. Xu, K. Xian, B. Gao, J. Qin, J. Zhang, Z. Wei, J. Hou, Achieving over 15% efficiency in organic photovoltaic cells via copolymer design, Adv. Mater. 31(14) (2019) 1808356. https://doi.org/doi:10.1002/adma.201808356.

[20] Q. Kang, B. Yang, Y.e. Xu, B. Xu, J. Hou, Printable MoO_x anode interlayers for organic solar cells, Adv. Mater. 30 (35) (2018) 1801718, https://doi.org/10.1002/adma.v30.3510.1002/adma.201801718.

[21] G.J. Wang, T.G. Jiu, P.D. Li, J. Li, C.M. Sun, F.S. Lu, J.F. Fang, Preparation and characterization of MoO_3 hole-injection layer for organic solar cell fabrication and optimization, Sol. Energy Mater. Sol. Cells 120 (2014) 603–609, https://doi.org/10.1016/j.solmat.2013.10.002.

[22] X.W. Zhang, F.J. You, Q.H. Zheng, Z.L. Zhang, P. Cai, X.G. Xue, J. Xiong, J. Zhang, Solution-processed MoO_x hole injection layer towards efficient organic light-emitting diode, Org. Electron. 39 (2016) 43–49, https://doi.org/10.1016/j.orgel.2016.09.022.

[23] Y.P. Li, H.Z. Yu, X.X. Huang, Z.P. Wu, M.D. Chen, A simple synthesis method to prepare a molybdenum oxide hole-transporting layer for efficient polymer solar cells, RSC Adv. 7 (13) (2017) 7890–7900, https://doi.org/10.1039/c7ra00303j.

[24] J.J. Jasieniak, J. Seifter, J. Jo, T. Mates, A.J. Heeger, A solution-processed MoO_x anode interlayer for use within organic photovoltaic devices, Adv. Funct. Mater. 22 (12) (2012) 2594–2605, https://doi.org/10.1002/adfm.201102622.

[25] H.N. Tran, S. Park, F.T.A. Wibowo, N.V. Krishna, J.H. Kang, J.H. Seo, H. Nguyen-Phu, S.-Y. Jang, S. Cho, 17% non-fullerene organic solar cells with annealing-free aqueous MoO_x, Adv. Sci. 7 (21) (2020) 2002395, https://doi.org/10.1002/advs.v7.2110.1002/advs.202002395.

[26] S.R. Hammond, J. Meyer, N.E. Widjonarko, P.F. Ndione, A.K. Sigdel, A. Garcia, A. Miedaner, M.T. Lloyd, A. Kahn, D.S. Ginley, J.J. Berry, D.C. Olson, Low-temperature, solution-processed molybdenum oxide hole-collection layer for organic photovoltaics, J. Mater. Chem. 22 (7) (2012) 3249–3254, https://doi.org/10.1039/c2jm14911g.

[27] Y. Gong, Y. Dong, B. Zhao, R. Yu, S. Hu, Z.A. Tan, Diverse applications of MoO_3 for high performance organic photovoltaics: fundamentals, processes and optimization strategies, J. Mater. Chem. A 8 (3) (2020) 978–1009, https://doi.org/10.1039/C9TA12005J.

[28] W. Pan, Y. Han, Z. Wang, Q. Luo, C. Ma, L. Ding, Over 1 cm^2 flexible organic solar cells, J. Semicond. 42 (5) (2021) 050301, https://doi.org/10.1088/1674-4926/42/5/050301.

[29] K. Inzani, M. Nematollahi, S.M. Selbach, T. Grande, M.L. Waalekalv, T. Brakstad, T. W. Reenaas, M. Kildemo, F. Vullum-Bruer, Tailoring properties of nanostructured MoO_{3-x} thin films by aqueous solution deposition, Appl. Surf. Sci. 459 (2018) 822–829, https://doi.org/10.1016/j.apsusc.2018.07.196.

[30] C. Lu, Rusli, A.B. Prakoso, Z. Li, Investigation of solution processed molybdenum oxide as selective contacts for silicon solar cells application, Mater. Chem. Phys. 236 (2019) 121779, https://doi.org/10.1016/j.matchemphys.2019.121779.

[31] B. Yang, Y.u. Chen, Y. Cui, D. Liu, B. Xu, J. Hou, Over 100-nm-thick MoO_x films with superior hole collection and transport properties for organic solar cells, Adv. Energy Mater. 8 (25) (2018) 1800698, https://doi.org/10.1002/aenm.v8.2510.1002/aenm.201800698.

[32] Q. Gao, S. Wang, H. Fang, J. Weng, Y. Zhang, J. Mao, Y. Tang, One-dimensional growth of MoO_x-based organic–inorganic hybrid nanowires with tunable photochromic properties, J. Mater. Chem. 22 (11) (2012) 4709, https://doi.org/10.1039/c2jm15443a.

[33] H. Yu, Z. Zhuang, D. Li, Y. Guo, Y. Li, H. Zhong, H. Xiong, Z. Liu, Z. Guo, Photo-induced synthesis of molybdenum oxide quantum dots for surface-enhanced Raman scattering and photothermal therapy, J. Mater. Chem. B 8 (5) (2020) 1040–1048, https://doi.org/10.1039/c9tb02102g.

[34] X.-X. Liu, L.-J. Bian, L. Zhang, L.-J. Zhang, Composite films of polyaniline and molybdenum oxide formed by electrocodeposition in aqueous media, J. Solid. State. Electrochem. 11 (9) (2007) 1279–1286, https://doi.org/10.1007/s10008-007-0287-3.

[35] F. Xie, W.C.H. Choy, C. Wang, X. Li, S. Zhang, J. Hou, Low-temperature solution-processed hydrogen molybdenum and vanadium bronzes for an efficient hole-transport layer in organic electronics, Adv. Mater. 25 (14) (2013) 2051–2055, https://doi.org/10.1002/adma.201204425.

[36] Y. Wang, Q. Luo, N. Wu, Q. Wang, H. Zhu, L. Chen, Y.Q. Li, L. Luo, C.Q. Ma, Solution-processed MoO_3:PEDOT:PSS hybrid hole transporting layer for inverted polymer solar cells, ACS Appl. Mater. Interfaces 7 (13) (2015) 7170–7179, https://doi.org/10.1021/am509049t.

[37] O. Oderinde, I. Hussain, M. Kang, Y. Wu, K. Mulenga, I. Adebayo, F. Yao, G. Fu, Water as des-cosolvent on the morphology tuning and photochromic enhancement of tungsten oxide-molybdenum oxide nanocomposite, J. Ind. Eng. Chem. 80 (2019) 1–10, https://doi.org/10.1016/j.jiec.2019.07.023.

[38] Z.A. Tan, D.P. Qian, W.Q. Zhang, L.J. Li, Y.Q. Ding, Q. Xu, F.Z. Wang, Y.F. Li, Efficient and stable polymer solar cells with solution-processed molybdenum oxide interfacial layer, J. Mater. Chem. A 1 (3) (2013) 657–664, https://doi.org/10.1039/c2ta00325b.

[39] S. Jung, J. Lee, U. Kim, H. Park, Solution-processed molybdenum oxide with hydroxyl radical-induced oxygen vacancy as an efficient and stable interfacial layer for organic solar cells, Sol. RRL 4 (3) (2020) 1900420, https://doi.org/10.1002/solr.v4.310.1002/solr.201900420.

[40] L. Sun, W. Zeng, C. Xie, L. Hu, X. Dong, F. Qin, W. Wang, T. Liu, X. Jiang, Y. Jiang, Y. Zhou, Flexible all-solution-processed organic solar cells with high-performance nonfullerene active layers, Adv. Mater. 32 (14) (2020) 1907840, https://doi.org/10.1002/adma.v32.1410.1002/adma.201907840.

[41] L. Xie, Q. Zhu, G. Zhang, K.e. Ye, C. Zou, O.V. Prezhdo, Z. Wang, Y.i. Luo, J. Jiang, Tunable hydrogen doping of metal oxide semiconductors with acid–metal treatment at ambient conditions, J. Am. Chem. Soc. 142 (9) (2020) 4136–4140, https://doi.org/10.1021/jacs.0c0056110.1021/jacs.0c00561.s001.

[42] I. Ismail, J. Wei, X. Sun, W. Zha, M. Khalil, L. Zhang, R. Huang, Z. Chen, Y. Shen, F. Li, Q. Luo, C.Q. Ma, Simultaneous improvement of the long-term and thermal stability of the perovskite solar cells using 2,3,4,5,6-pentafluorobenzoyl chloride (PFBC)-capped ZnO nanoparticles buffer layer, Sol. RRL 4 (10) (2020) 1–12, https://doi.org/10.1002/solr.202000289.

[43] G. Ji, Y. Wang, Q. Luo, K. Han, M. Xie, L. Zhang, N.a. Wu, J. Lin, S. Xiao, Y.-Q. Li, L.-Q. Luo, C.-Q. Ma, Fully coated semitransparent organic solar cells with a doctor-blade-coated composite anode buffer layer of phosphomolybdic acid and PEDOT:PSS and a spray-coated silver nanowire top electrode, ACS Appl. Mater. Interfaces 10 (1) (2018) 943–954, https://doi.org/10.1021/acsami.7b1334610.1021/acsami.7b13346.s001.

[44] S. Dong, Z. Hu, K. Zhang, Q. Yin, X. Jiang, F. Huang, Y. Cao, Cross-linkable and dual functional hybrid polymeric electron transporting layer for high-performance inverted polymer solar cells, Adv. Mater. 29 (34) (2017) 1701507, https://doi.org/10.1002/adma.v29.3410.1002/adma.201701507.

[45] X. Liu, X. Li, Y. Li, C. Song, L. Zhu, W. Zhang, H.Q. Wang, J. Fang, High-performance polymer solar cells with PCE of 10.42% via Al-doped ZnO cathode interlayer, Adv. Mater. 28(34) (2016) 7405-7412. https://doi.org/10.1002/adma.201601814.

[46] R. Singh, R. Sivakumar, S.K. Srivastava, T. Som, Growth angle-dependent tunable work function and optoelectronic properties of MoO_x thin films, Appl. Surf. Sci. 507 (2020) 144958, https://doi.org/10.1016/j.apsusc.2019.144958.

[47] M. Rouhani, Y.L. Foo, J. Hobley, J. Pan, G.S. Subramanian, X. Yu, A. Rusydi, S. Gorelik, Photochromism of amorphous molybdenum oxide films with different initial Mo^{5+} relative concentrations, Appl. Surf. Sci. 273 (2013) 150–158, https://doi.org/10.1016/j.apsusc.2013.01.218.

[48] T. He, J.N. Yao, Photochromism of molybdenum oxide, J. Photoch. Photobio. C 4 (2) (2003) 125–143, https://doi.org/10.1016/S1389-5567(03)00025-X.

[49] N. Li, Y. Li, G. Sun, Y. Zhou, S. Ji, H. Yao, X. Cao, S. Bao, P. Jin, Enhanced photochromic modulation efficiency: a novel plasmonic molybdenum oxide hybrid, Nanoscale 9 (24) (2017) 8298–8304, https://doi.org/10.1039/c7nr02763j.

[50] M. Rouhani, S. Gorelik, J. Hobley, S.J. Wang, E.L. Williams, Y.L. Foo, Delayed onset of photochromism in molybdenum oxide films caused by photoinduced defect formation, Sci. Technol. Adv. Mater. 12 (5) (2011) 055010, https://doi.org/10.1088/1468-6996/12/5/055010.

[51] M. Rouhani, J. Hobley, G.S. Subramanian, I.Y. Phang, Y.L. Foo, S. Gorelik, The influence of initial stoichiometry on the mechanism of photochromism of

molybdenum oxide amorphous films, Sol. Energy Mater. Sol. Cells 126 (2014) 26–35, https://doi.org/10.1016/j.solmat.2014.03.033.

[52] N. Li, Y. Li, W. Li, S. Ji, P. Jin, One-step hydrothermal synthesis of TiO_2@MoO_3 core–shell nanomaterial: microstructure, growth mechanism, and improved photochromic property, J. Phys. Chem. C 120 (6) (2016) 3341–3349, https://doi.org/10.1021/acs.jpcc.5b1075210.1021/acs.jpcc.5b10752.s001.

[53] Y. Chen, F. Bai, Z. Peng, L. Zhu, J. Zhang, X. Zou, Y. Qin, H.K. Kim, J. Yuan, L.-K. Ma, J. Zhang, H. Yu, P.C.Y. Chow, F. Huang, Y. Zou, H. Ade, F. Liu, H.e. Yan, Asymmetric alkoxy and alkyl substitution on nonfullerene acceptors enabling high-performance organic solar cells, Adv. Energy Mater. 11 (3) (2021) 2003141, https://doi.org/10.1002/aenm.v11.310.1002/aenm.202003141.

[54] C. Zhu, J. Yuan, F. Cai, L. Meng, H. Zhang, H. Chen, J. Li, B. Qiu, H. Peng, S. Chen, Y. Hu, C. Yang, F. Gao, Y. Zou, Y. Li, Tuning the electron-deficient core of a non-fullerene acceptor to achieve over 17% efficiency in a single-junction organic solar cell, Energy Environ. Sci. 13 (8) (2020) 2459–2466, https://doi.org/10.1039/D0EE00862A.

[55] H. Gu, L. Yan, S. Saxena, X. Shi, X. Zhang, Z. Li, Q. Luo, H. Zhou, Y. Yang, X. Liu, W. W.H. Wong, C.-Q. Ma, Revealing the interfacial photoreduction of MoO_3 with P3HT from the molecular weight-dependent "Burn-in" degradation of P3HT: $PC_{61}BM$ solar cells, ACS Appl. Energy Mater. 3 (10) (2020) 9714–9723, https://doi.org/10.1021/acsaem.0c0132510.1021/acsaem.0c01325.s001.